Microstructure evolution of $Zr_2Al_3C_4$ in Cu matrix

J. Zhang
Shenyang National Laboratory for Materials Science, Institute of Metal Research, Chinese Academy of Sciences, Shenyang 110016, China; and Graduate School of Chinese Academy of Sciences, Beijing 100039, China

J.Y. Wang and Y.C. Zhou[a)]
Shenyang National Laboratory for Materials Science, Institute of Metal Research, Chinese Academy of Sciences, Shenyang 110016, China

(Received 9 July 2010; accepted 21 September 2010)

Interfacial reaction and microstructure evolution in a $Zr_2Al_3C_4$ reinforced Cu composite were studied by x-ray diffraction, Raman spectroscopy, and transmission electron microscopy. Decomposition of $Zr_2Al_3C_4$ was triggered by the deintercalation of Al atoms. In the initial reaction stage, depletion of Al occurred locally. ZrC and Cu platelets as well as thin twinned ZrC slices were observed inside the $Zr_2Al_3C_4$ grains. In the later reaction stage, all Al atoms depleted from $Zr_2Al_3C_4$ and were dissolute into the Cu matrix. The final reaction products were a Cu–Al solid solution, $ZrC_{0.5}$, and highly disordered graphite, which resulted in large volume shrinkage. These experimental results provided a baseline for controlling interfacial reaction and microstructure development in Cu/$Zr_2Al_3C_4$-based particle-reinforced Cu composites for optimized mechanical and electrical properties.

I. INTRODUCTION

Copper (Cu) has widespread applications, such as heat exchangers, make-and-break electric switches, and sliding contact materials, due to its good electrical and thermal conductivities.[1,2] The lack of strength and wear resistance, however, limits the extensive usage of pure Cu. Ceramic particle-reinforced Cu matrix composite combines the good electrical conductivity and ductility of metal matrix with the high strength and modulus of ceramic reinforcement, leading to better mechanical behaviors and higher service temperatures. Therefore, a variety of ceramics such as SiC, Al_2O_3, and TiB_2[3–6] have been added into the Cu matrix.

Recently, a family of layered ternary carbides, namely MAX phases (where M is a transition metal, A is a group IIIA to IVA element, and X is C or N), have attracted extensive interest mainly because of their fascinating electrical, thermal, and mechanical properties.[7–9] When these carbides, Ti_3AlC_2 or Ti_3SiC_2 for instance, were added into Cu, significant improvements in both hardness and strength were obtained without much loss of the electrical conductivity.[10–12] Because of the similarity in their crystal structures, another family of layered carbides with the formula of $T_nAl_3C_{n+2}$ or $T_nAl_4C_{n+3}$ (where T is Zr or Hf, n = 1, 2, and 3)[13,14] can also be added into Cu to achieve similar or better effects. Among the Zr–Al–C systems, $Zr_2Al_3C_4$ is the most attractive member, which possesses higher modulus, strength, and hardness than those of Ti_3AlC_2.[15–18] In the previous work, we synthesized a highly conductive and strengthened Cu matrix composite by adding $Zr_2Al_3C_4$ particles.[19] The electrical conductivity of the Cu/$Zr_2Al_3C_4$ composite is comparable to that of Cu/graphite, which has been extensively used in sliding electrical contact applications, while the Cu/$Zr_2Al_3C_4$ composite possesses superior mechanical properties.

Although bulk $Zr_2Al_3C_4$ ceramic has higher strength and hardness than those of Ti_3AlC_2, the tensile strength of Cu/$Zr_2Al_3C_4$ composite is much lower than that of Cu/Ti_3AlC_2 composite. In the Cu/Ti_3AlC_2 composite,[20] a high-strength interfacial layer composed of Cu–Al solid solution and TiC_x forms, which helps to transfer the load from the matrix to the reinforcement. In the newly developed Cu/$Zr_2Al_3C_4$ composite, $Zr_2Al_3C_4$ particles are mechanically gripped by Cu matrix,[19] which does not favor the load transfer and results in the limited strengthening effects. Because the microstructures and properties of materials are generally related, characterizing and understanding the microstructure evolution are essential for optimizing the processing parameters and performance of Cu/$Zr_2Al_3C_4$ composite. In addition, braze is a common jointing material between ultrahigh temperature ceramic and metal.[21–24] Understanding the reaction between $Zr_2Al_3C_4$ and Cu matrix will also help to evaluate the joining between $Zr_2Al_3C_4$ and Cu, enabling applications of $Zr_2Al_3C_4$ as high-temperature coatings.

In this work, we investigate the structure stability of $Zr_2Al_3C_4$ in a Cu matrix by annealing the as-synthesized Cu/30 vol%$Zr_2Al_3C_4$ samples in the temperature range

[a)]Address all correspondence to this author.
e-mail: yczhou@imr.ac.cn
DOI: 10.1557/jmr.2010.52

 © Materials Research Society 2011

https://doi.org/10.1557/jmr.2010.52 Published online by Cambridge University Press

from 850 to 1050 °C. The structure stability of two binary carbides related to $Zr_2Al_3C_4$, i.e., Al_4C_3 and ZrC, are also studied by annealing the as-synthesized Cu/30 vol%Al_4C_3 and Cu/30 vol%ZrC samples. Finally, implications to microstructure optimization of Cu matrix composites are discussed.

II. EXPERIMENTAL

A near fully dense Cu/30 vol%$Zr_2Al_3C_4$ sample was prepared by the powder metallurgy method. The sintering temperature was set to be 850 °C; details of the experimental procedure are described in Ref. 19. To investigate the microstructure evolution, the as-prepared Cu/30 vol% $Zr_2Al_3C_4$ samples were annealed at 850, 900, 950, 1000, and 1050 °C, respectively, with a soaking time of 20, 40, and 60 min, respectively, in a tube furnace with flowing Ar gas. To investigate the structure stability of the related binary carbides, Al_4C_3 and ZrC powders synthesized in our lab were mixed with Cu powder to prepare Cu/30 vol %Al_4C_3 and Cu/30 vol%ZrC composites. These samples were then annealed under the conditions identical to those of Cu/30 vol%$Zr_2Al_3C_4$ samples.

The phase evolution of the annealed samples was characterized by x-ray diffraction (XRD) and Raman spectroscopy. The XRD data were collected using a diffractometer (Rigaku D/max-2500PC, Tokyo, Japan) in the step-scanning mode with Cu K_α radiation (λ = 1.541 Å). The scanning speed was 0.04° per step. The Raman spectra were measured at room temperature in a Raman spectrometer (JY LabRam HR 800, Longjumeau, France) using a He-Ne laser with a wavelength of 632.8 nm as the excitation source.

Microstructure evolution of $Zr_2Al_3C_4$ in Cu was investigated using transmission electron microscopy (TEM). TEM specimens were prepared by slicing, mechanical grinding (down to ~30 μm), dimpling (down to ~10 μm), and ion beam milling at 4 kV. A Tecnai G^2 F30 microscope (FEI, Eindhoven, The Netherlands) was used for TEM imaging. Fast Fourier transformation (FFT) was carried out using a DigitalMicrograph software package (Gatan Inc., Pleasanton, CA). Interfacial models were built on the basis of the observed interfacial structures using the Interfacial Builder code in the Cerius^2 computational program (Molecular Simulation Inc., San Diego, CA).

III. RESULTS

A. Structure stability of $Zr_2Al_3C_4$ in Cu matrix

1. Phase evolution of Cu/$Zr_2Al_3C_4$ composites at high temperatures

In the as-prepared Cu/30 vol%$Zr_2Al_3C_4$ composite, $Zr_2Al_3C_4$ particles are uniformly distributed in Cu matrix. Figure 1 shows the XRD patterns of the as-prepared and annealed samples. In the as-prepared sample, only $Zr_2Al_3C_4$ and Cu are identified [Fig. 1(a)]; these two phases remain unchanged after annealing up to 900 °C [Fig. 1(b)]. When the annealing temperature reaches 950 °C, an apparent reaction between Cu and $Zr_2Al_3C_4$ occurs. After annealing at 950 °C for 40 min, Cu peaks shift to low angles [Fig. 1(c)], indicating the formation of a Cu–Al solid solution; this is because Cu has high affinity to Al at high temperatures and the lattice constant of Cu–Al solid solution is larger than that of pure Cu. The XRD pattern shown in Fig. 1(c) also indicates the precipitation of a small amount of ZrC. Consistently, the intensity of $Zr_2Al_3C_4$ reflections decreases [Fig. 1(c)]. Prolonged annealing at 950 °C results in further reduction of the intensity of $Zr_2Al_3C_4$ reflections in conjunction with an increase of the intensity of ZrC peaks and a further shift of Cu peaks toward low angles [Fig. 1(d)]. When the annealing temperature reaches 1050 °C, only ZrC and Cu are detected by XRD [Fig. 1(e)], which indicates the completion of the $Zr_2Al_3C_4$ decomposition.

Lattice constants of Cu and ZrC in the samples treated under different conditions are measured and listed in Table I. It can be seen that with the increase of annealing temperature and annealing time, the lattice constant of Cu increases. Extensive reports[25–27] on the dependence of lattice constants of Cu–Al solid solution are summarized in Fig. 2(a). By linear fitting of the measured lattice constants of Cu into Obinata et al.[25] and Bardley et al.[26] results, the calculated solid solubility of Al in Cu under different annealing conditions are obtained [marked with stars in Fig. 2(a) and listed in Table I]. For the sample annealed at 1050 °C for 60 min, the Al fraction in the solid solution is calculated to be 12 at.%. Theoretically, if all Al in Cu/30 vol%$Zr_2Al_3C_4$ sample dissolves into Cu matrix,

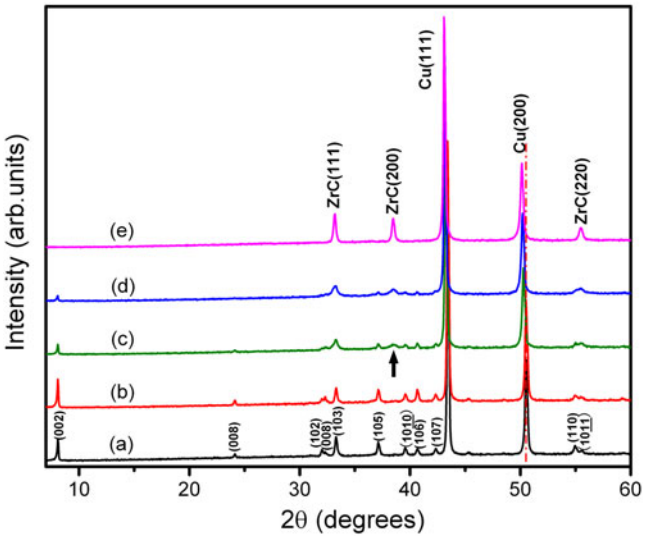


FIG. 1. XRD patterns of (a) as-prepared Cu/30 vol%$Zr_2Al_3C_4$ sample and those annealed at (b) 900 °C for 60 min, (c) 950 °C for 40 min, (d) 950 °C for 60 min, and (e) 1050 °C for 60 min, respectively.

https://doi.org/10.1557/jmr.2010.52 Published online by Cambridge University Press

the Al fraction should be 12.3 at.%. With the experimental errors, this is essentially identical to the fitted experimental result. According to the Al–Cu binary phase diagram, the solid solubility limit of Al in Cu is around 18 at.%; thus, no Cu–Al intermetallic phase should form during annealing. Therefore, it is concluded that after annealing at 1050 °C for 60 min, all Al dissolve into the matrix.

If $Zr_2Al_3C_4$ merely undergoes the depletion of Al (without changing the Zr/C ratio), the resultant ZrC will depart from its stoichiometry. It was reported that the stoichiometry of ZrC varied in a wide range from $ZrC_{0.45}$ to $ZrC_{0.95}$.[28–30] A few works studied the variation of lattice constants of ZrC_x with the substoichiometry,[31,32] but there is a significant difference among the results [shown in Fig. 2(b)]. Because the lattice constant of $ZrC_{1.0}$ (a = 4.694 Å) from Ref. 31 matches with the JCPDS (PDF Card No. 730477), the lattice constant of ZrC_x in this work is linearly fitted according to it. It is found that the reaction product, ZrC, is understoichiometrc in C with the formula of $ZrC_{0.54}$ [marked in Fig. 2(b)]. Taking into account the mass conservation, the reaction between $Zr_2Al_3C_4$ and Cu can be described as

$$Zr_2Al_3C_4 + Cu \rightarrow Cu{-}Al \text{ solid solution} + 2\,ZrC_{0.5} + 2\,C \quad .$$

Compared with XRD patterns, Raman spectrum is suitable to detect the presence of graphite.[33] In Fig. 3(a), sharp and intensive peaks at 108, 148, 183, 253, 418, and 633 cm^{-1} are clearly detected for the as-prepared Cu/30 vol%$Zr_2Al_3C_4$ sample, which is presumed to be characteristic Raman peaks of $Zr_2Al_3C_4$.[34] After annealing at 1050 °C for 60 min, only two peaks at higher wave numbers, i.e., 1331 and 1586 cm^{-1} can be distinguished [Fig. 3(b)], which correspond to the D and G modes of carbon. Single crystalline graphite has a single Raman active mode, a zone-center mode at 1580 cm^{-1} of E_{2g} symmetry [labeled "G" for "graphite" in Fig. 3(b)]. Disordered graphite has a second vibration mode at around 1350 cm^{-1} of A_{1g} symmetry (labeled "D" for "disorder").[35] Consequently, the intensity ratio of the D and G modes, I(D)/I(G), which varied inversely with the in-plane correlation length L_a of the graphite,[36] revealed the disordering of graphite. The intensity ratio of the D and G modes in Fig. 3(b) is 1.70, which indicates that the graphite resulted from decomposition of $Zr_2Al_3C_4$ is highly disordered with small in-plane correlation length.

2. Stability of Al_4C_3 and ZrC in Cu at high temperatures

The crystal structure of $Zr_2Al_3C_4$ is shown in Fig. 4. It crystallizes in the space group of $P6_3/mmc$,[37,38] with an intergrowth of two alternatively basic units—a Zr–C slab with C atoms in octahedral Zr coordination and a Al–C slab. These two slabs share the carbon-atom network at

TABLE I. Lattice constants of Cu and ZrC in the samples under different annealing conditions.

Material	Lattice constant of Cu (Å)	Solid solubility of Al in Cu (at.%)	Lattice constant of ZrC (Å)
As-prepared Cu/30 ZAC	3.611	...	...
850 °C for 60 min	3.611	...	...
950 °C for 40 min	3.629	8.7	...
950 °C for 60 min	3.631	9.8	4.673
1050 °C for 60 min	3.636	12.0	4.678

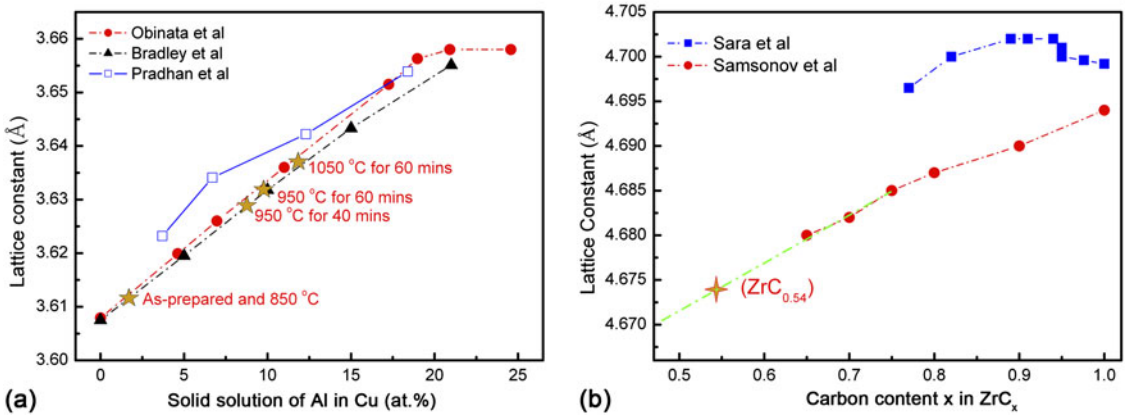


FIG. 2. (a) Measured lattice constants of Cu–Al solid solution variation as Al solubility from Refs. 25–27 and the results of this work (marked with stars), (b) lattice constants of cubic ZrC_x as a function of carbon content in Refs. 28 and 29 and the results of this work (marked with stars).

https://doi.org/10.1557/jmr.2010.52 Published online by Cambridge University Press

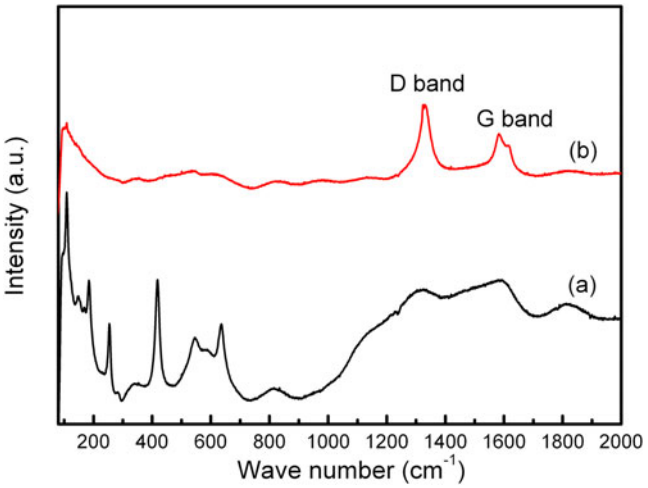


FIG. 3. Raman spectra of (a) as-prepared Cu/30 vol%$Zr_2Al_3C_4$ sample and (b) sample annealed at 1050 °C for 60 min.

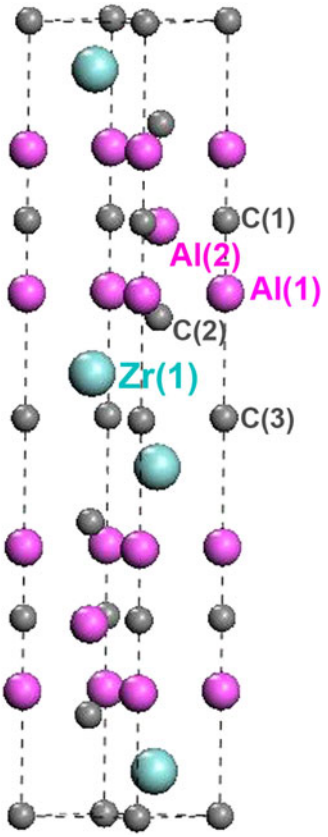


FIG. 4. Crystal structure of $Zr_2Al_3C_4$.

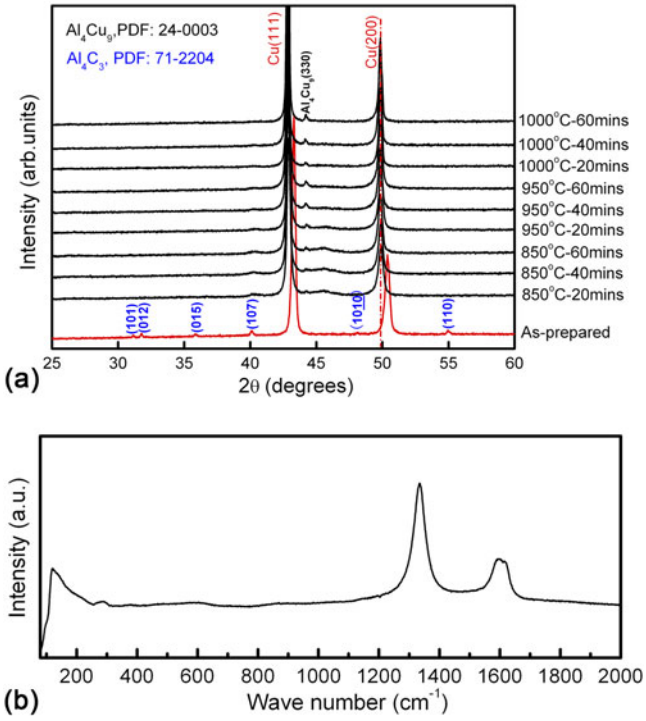


FIG. 5. (a) XRD patterns of the as-synthesized Cu/30 vol%Al_4C_3 sample and those after annealed under different conditions, (b) Raman spectra of the Cu/30 vol%Al_4C_3 sample annealed at 1000 °C for 60 min.

their boundaries and the atomic bonding characteristic of the Zr_2C and Al_3C_2 units in $Zr_2Al_3C_4$ are similar to those in ZrC and Al_4C_3, respectively. Evaluating the structure stability of Al_4C_3 and ZrC will help to understand the stability of Zr_2C and Al_3C_2 units in $Zr_2Al_3C_4$. Therefore, the as-synthesized Cu/30 vol%Al_4C_3 and Cu/30 vol%ZrC samples are annealed under the conditions identical to that of Cu/30 vol%$Zr_2Al_3C_4$ samples.

The XRD patterns of the as-synthesized and annealed Cu/30 vol%Al_4C_3 samples are presented in Fig. 5(a). In the as-synthesized sample, the peaks that belong to Al_4C_3 and Cu can be identified clearly. After annealing at 850 °C for 20 min, the Cu peaks shift to low angles, indicating the dissolution of Al into Cu matrix. With the increase of the annealing temperature and time, the Al_4Cu_9 phase emerges and the position of Cu peaks remains unchanged. If all Al in the Cu/30 vol%Al_4C_3 sample dissolves into Cu, the solid solubility is 21.6 at.%, which is already over the solid solubility limit of Al in Cu. Consequently, intermetallic compound forms as the reaction product. Since ZrC is stable in contact with Cu, no reaction occurs in Cu/30 vol%ZrC composite in the whole temperature ranges (not shown here).

Raman analysis is also performed to characterize the Cu/30 vol%Al_4C_3 sample after annealing at 1000 °C for 60 min and the result is presented in Fig. 5(b). Only two peaks at 1334 and 1584 cm^{-1} can be distinguished, which correspond to the D and G modes of graphite, respectively. The intensity ratio of the D and G modes in Fig. 5(b) is analogue to the spectrum shown in Fig. 3(b). The graphite from the decomposition of Al_4C_3 is also highly disordered with a small in-plane correlation length, which provides

https://doi.org/10.1557/jmr.2010.52 Published online by Cambridge University Press

the evidence that the graphite resulting from decomposition of $Zr_2Al_3C_4$ is from the Al–C unit in its crystal structure.

Al_4C_3 is known as the only intermediate compound in the Al–C binary system and extensive investigations of its stability were performed.[39–41] In this work, it is interesting to notice that Al_4C_3 reacts with Cu at lower temperatures than that for $Zr_2Al_3C_4$. The structure stability difference of the Al–C units in Al_4C_3 and $Zr_2Al_3C_4$ can be explained in view of the atomic bonding. The ideal tensile strength reflects the atomic bonding strength between atoms. The ideal tensile strength of Al–C bond in $Zr_2Al_3C_4$ is calculated to be 26.8 GPa.[42,43] Calculation is also performed on Al_4C_3 using an identical method, and the calculated ideal tensile strength is only 21 GPa.[44] In other words, the atomic bonding between Al and C atoms becomes stronger when the Al–C unit intercalates with the Zr–C unit to form $Zr_2Al_3C_4$. Therefore, ternary carbide $Zr_2Al_3C_4$ exhibits higher stability than Al_4C_3 in Cu matrix.

B. Typical microstructure of Cu/$Zr_2Al_3C_4$ composite during annealing

The aforementioned results suggest that the decomposition of $Zr_2Al_3C_4$ is triggered by the depletion of Al atoms accompanied with the formation of $ZrC_{0.5}$ and graphite. To reveal the microstructure evolution of Cu/$Zr_2Al_3C_4$ composite during annealing, the as-prepared Cu/30 vol%$Zr_2Al_3C_4$ sample and those annealed at 950 and 1050 °C for 60 min were analyzed by TEM.

Figure 6(a) indicates the microstructure of the as-synthesized Cu/30 vol%$Zr_2Al_3C_4$ sample. No reaction between $Zr_2Al_3C_4$ and Cu are observed. The high-resolution TEM (HRTEM) lattice image of the interface is shown in Fig. 6(b). The $Zr_2Al_3C_4$ grain orients in the $[1\bar{2}10]$ zone axis and the interface is parallel to its basal plane. No low-index orientation relationship exists between Cu and $Zr_2Al_3C_4$; therefore, only weak fringes of the Cu (110) plane are visible. At the interface, an amorphous layer links Cu and $Zr_2Al_3C_4$ grains. Further analysis finds the presence of the O, Cu, and a small amount of Zr and Al.

When the annealing temperature reaches 950 °C, pores and thin ZrC platelets are observed inside $Zr_2Al_3C_4$ grain, as indicated in Fig. 7(a). The formation of ZrC microtwins is also revealed by the selected-area electron diffraction (SAED) pattern shown in Fig. 7(b). Compared with XRD, TEM is able to display the crystallographic and morphological information from small domains. The alternating distributions of ZrC and Cu platelets as well as thin ZrC twins are observed inside $Zr_2Al_3C_4$ grain [Figs. 7(c) and 7(d)].

Increasing the annealing temperature to 1050 °C, there is no $Zr_2Al_3C_4$ detected in the sample, which is consistent with the XRD result. The main phases are cubic ZrC and Cu. Both phases are highly twinned and present a lamellar structure, as shown in Fig. 8(a). As shown in the SAED pattern in Fig. 8(b), the following orientation relationship between ZrC and Cu exists

$$[1\bar{1}0]\,\mathrm{ZrC} /\!/ [1\bar{1}0]\,\mathrm{Cu} \quad ,$$

$$(hkl)\,\mathrm{ZrC} /\!/ (hkl)\,\mathrm{Cu}\ (h,\ k,\ l\ \text{are all odd or all even}) \quad .$$

This kind of cube-on-cube orientation relationship is likely produced by intergrowth of Cu and ZrC lamellas. The continuous distributions of ZrC and Cu twins as well as graphite are clearly identified in Figs. 8(c) and 8(d). Moiré patterns are also observed, which are formed by overlapping of Cu and ZrC platelets.

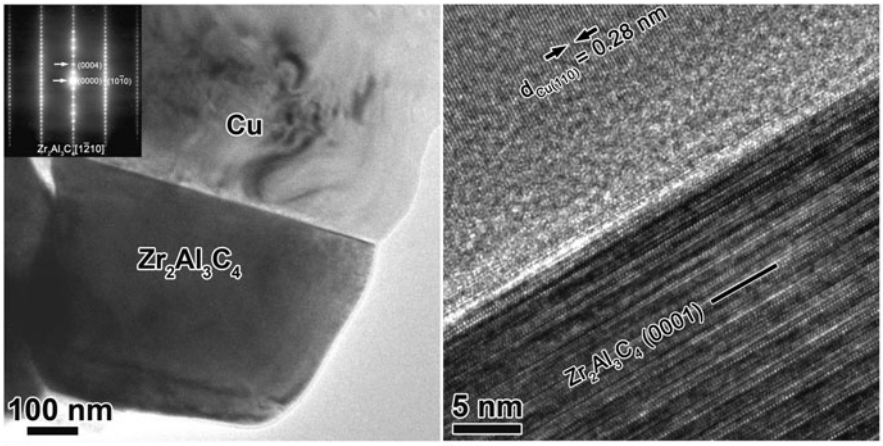


FIG. 6. (a) Typical microstructure of the as-synthesized Cu/30 vol%$Zr_2Al_3C_4$ sample and corresponding SAED pattern (inset), (b) HRTEM image of the $Zr_2Al_3C_4$ grain with the electron beam parallel to $[1\bar{2}10]$ direction.

https://doi.org/10.1557/jmr.2010.52 Published online by Cambridge University Press

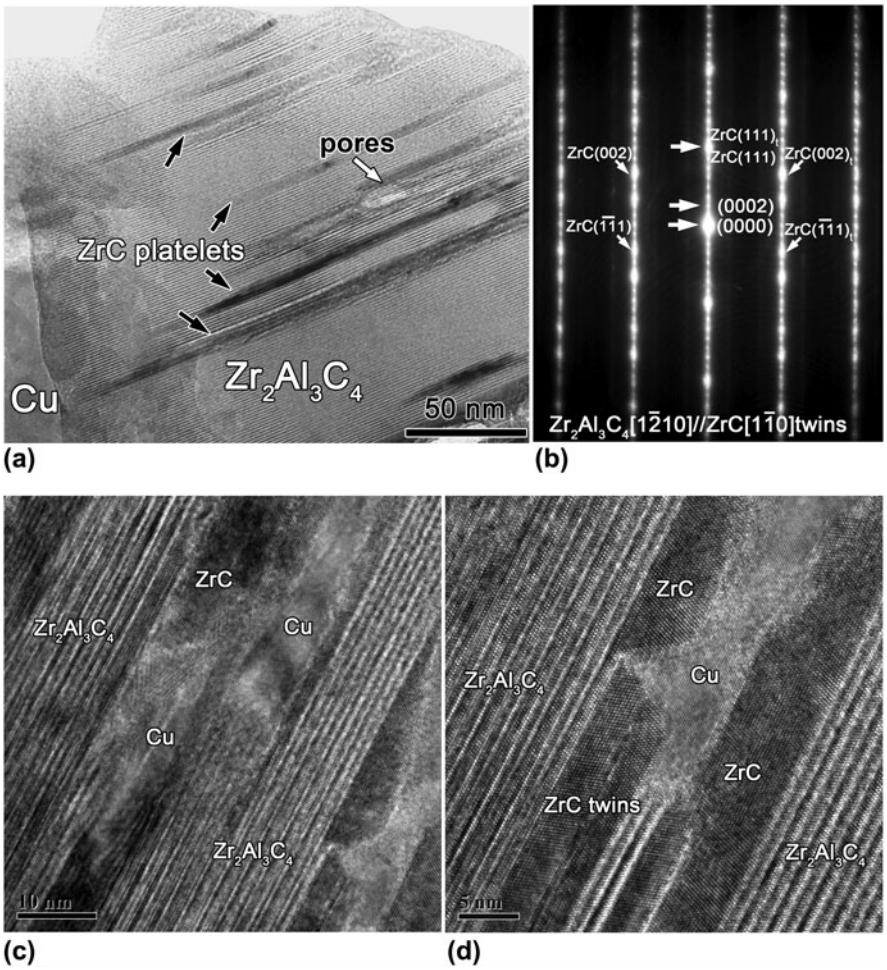


FIG. 7. (a) Typical morphology of $Zr_2Al_3C_4$ grain in the sample annealed at 950 °C, (b) corresponding SAED patterns, (c, d) HRTEM image of (a) in which $Zr_2Al_3C_4$, ZrC and Cu platelets as well as ZrC twins can be identified.

C. Microstructure evolution of $Zr_2Al_3C_4$ in Cu

The results in earlier sections have demonstrated that the reaction between $Zr_2Al_3C_4$ and Cu strongly depends on temperature. No reaction happens up to 950 °C. In the temperature range from 950 to 1000 °C mild reactions occur, Cu and ZrC coexist inside $Zr_2Al_3C_4$ grains. When the temperature reaches 1050 °C, highly twinned ZrC and Cu with alternating distributions form. With the help of Raman spectrum, highly disordered graphite is identified as another decomposition product of $Zr_2Al_3C_4$. Further investigations are necessary to understand the evolution of $Zr_2Al_3C_4$ in Cu at different temperatures.

1. Mild reaction between $Zr_2Al_3C_4$ and Cu

As shown in Fig. 7(a), mild reaction happens between $Zr_2Al_3C_4$ and Cu above 950 °C, resulting in the inner growth of ZrC, Cu, and pores inside $Zr_2Al_3C_4$ grains. The HRTEM image of the $Zr_2Al_3C_4$ grain is further enlarged [Fig. 9(a)], in which ZrC platelets distribute adjacent to $Zr_2Al_3C_4$. Further analysis shows that the orientation relationships between $Zr_2Al_3C_4$ and ZrC are different in the regions named "Interface I" and "Interface II," which are

$$\text{Interface I } [1\bar{2}10]\,Zr_2Al_3C_4 \,/\!/\, [1\bar{1}0]\,ZrC \quad ,$$

$$(0001)\,Zr_2Al_3C_4 \,/\!/\, (111)\,ZrC \quad ;$$

$$\text{Interface II } [1\bar{2}10]\,Zr_2Al_3C_4 \,/\!/\, [\bar{1}10]\,ZrC \quad ,$$

$$(0001)\,Zr_2Al_3C_4 \,/\!/\, (111)\,ZrC \quad .$$

To achieve better understandings of the structure relationship between $Zr_2Al_3C_4$ and ZrC, interfacial models are proposed in Figs. 9(b) and 9(c). In the regions named "Interface I" and "Interface II", ZrC lamellae adjoin to different planes of the ternary carbide, the interval of which is half a unit cell of $Zr_2Al_3C_4$. ZrC lamellae present mirror symmetrical arrangements with the adjacent $Zr_2Al_3C_4$ plane in both regions I and II. The formation

https://doi.org/10.1557/jmr.2010.52 Published online by Cambridge University Press

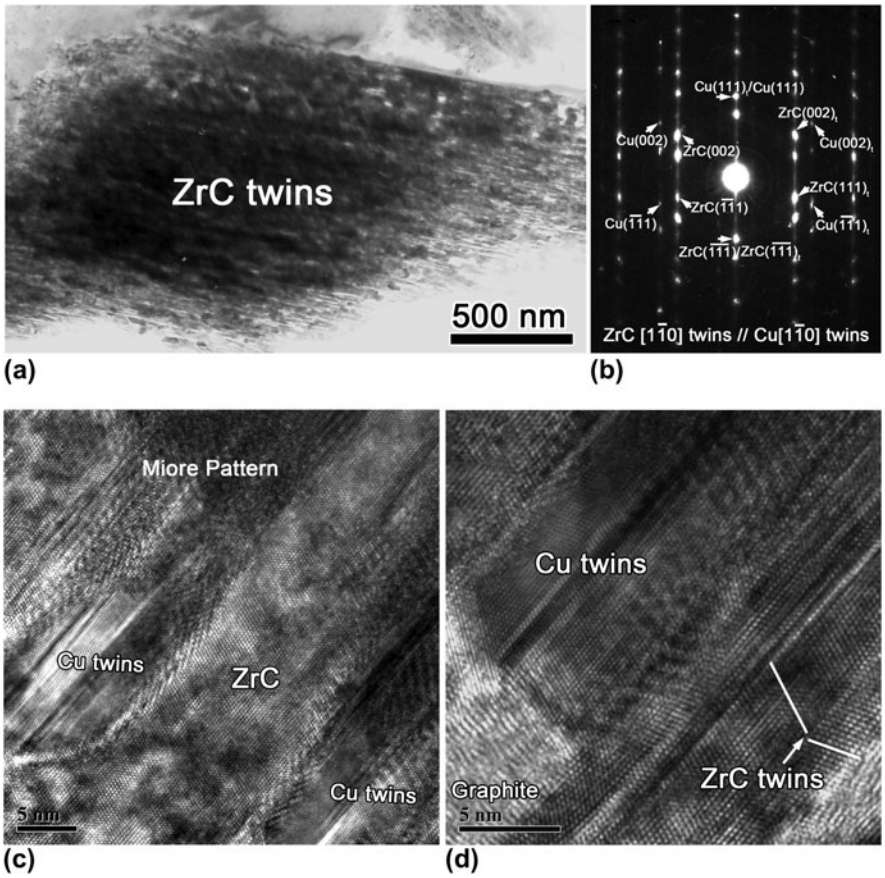


FIG. 8. (a) Characteristic morphology of $Zr_2Al_3C_4$ grains in the sample annealed at 1050 °C for 60 min, (b) corresponding SAED patterns of highly twined ZrC and Cu, (c, d) HRTEM images with alternative arrangements of ZrC and Cu twins.

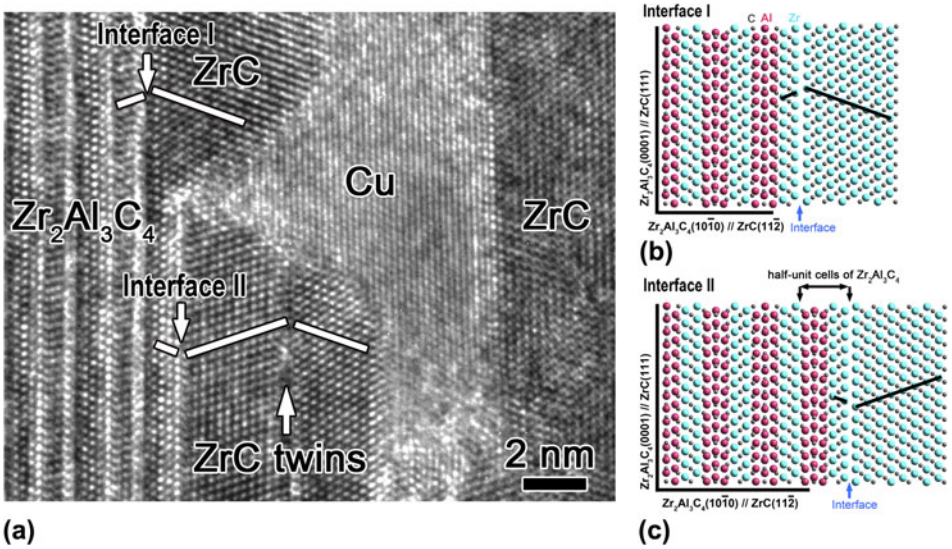


FIG. 9. HRTEM image shows (a) inner growth of ZrC and Cu platelets inside $Zr_2Al_3C_4$ grain, (b, c) interfacial models of "Interface I" and "Interface II."

of ZrC and Cu lamellae inside $Zr_2Al_3C_4$ grains are explained subsequently.

Projected on the (1$\bar{2}$10) plane, $Zr_2Al_3C_4$ can be described as two adjacent Zr–C–Zr chain and Al–C unit sharing C atoms, as clearly indicated in the left part of Figs. 9(b) and 9(c). When ZrC is projected on the (1$\bar{1}$0) plane, the Zr–C–Zr chain exhibits the same arrangement as that in $Zr_2Al_3C_4$. In the presence of Cu, which has an

https://doi.org/10.1557/jmr.2010.52 Published online by Cambridge University Press

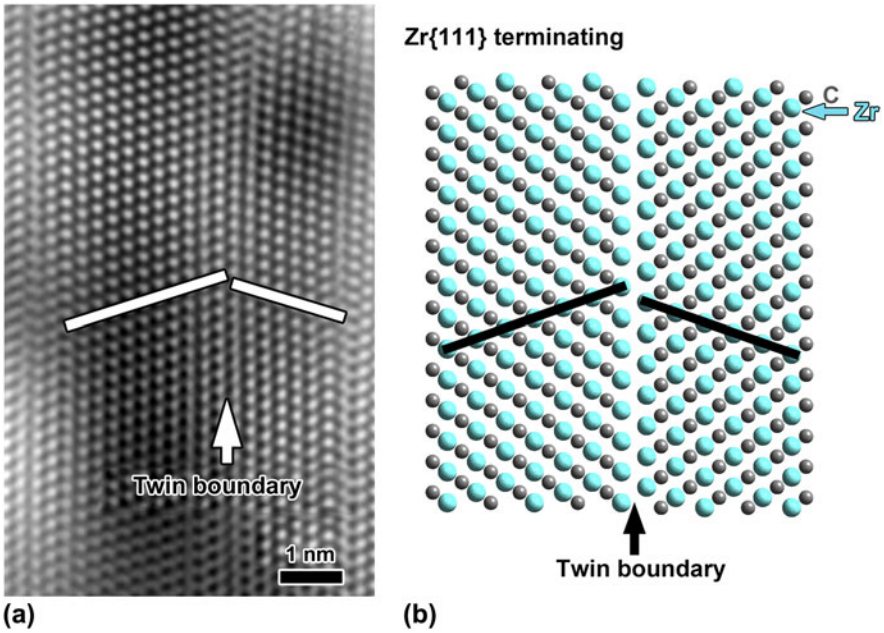


FIG. 10. (a) ZrC twins after image processing by Fourier filtering and (b) interface model of ZrC twin with Zr {111} terminating boundary.

affinity to Al at high temperatures, Al atoms deintercalate from $Zr_2Al_3C_4$, which destroys the entire Al–C unit and leaves a thin ZrC platelet. The depletion of Al–C unit causes volume shrinkage vertical to the basal plane of $Zr_2Al_3C_4$; therefore, the inner diffusion of Cu is easier. However, the volume shrinkage is quite large and pores are also observed inside $Zr_2Al_3C_4$ grains.

Directly abutting against Cu, a thin twinned ZrC slice is observed inside the $Zr_2Al_3C_4$ grain in the sample after mild reaction at 950 °C [Fig. 7(d)]. Figure 10(a) shows the enlarged and Fourier-filtered image of this twinned ZrC slice. The formation mechanism of ZrC twins is similar to that of TiC twins during reaction between Ti_3AlC_2 and Cu, which is sufficiently discussed in Ref. 20. In short, the NaCl-structured ZrC has two different {111} planes, which are denoted as Zr {111} and C {111}, respectively. Consequently, there are two possible types of ZrC (111) twin boundaries, i.e., Zr {111} terminating and C {111} terminating boundaries. In the C {111} terminating boundaries, C atoms bond adjacent Zr atoms equally, so the twin boundaries present a mirror symmetry. If Zr {111} terminates on both sides, a glide occurs as a result of the electrostatic repulsion between adjacent Zr atoms, as shown in Fig. 10(b). In this work, the ZrC_x is understoichiometric in C with the formula of $ZrC_{0.54}$, which enhance the direct bonding between Zr atoms.

2. Severe reaction between $Zr_2Al_3C_4$ and Cu

At 950 °C only a mild reaction occurs. With the annealing temperature increased to 1050 °C, severe reaction happens. Cu and cubic ZrC_x are the main phases. The resultant ZrC_x is understoichiometric in C with the formula of $ZrC_{0.54}$. Abundant C vacancies enhance the direct bonding between Zr atoms; therefore, the formation of ZrC twins is strongly promoted. Because the stacking fault energy of Cu is relatively low, twinning should be a common phenomenon. Consequently, Cu coexists with ZrC and both of them are highly twinned.

The decomposition of $Zr_2Al_3C_4$ into $ZrC_{0.54}$ accompanies with large volume shrinkage of ~52.5%. Consistently, a large number of pores are observed inside the ZrC grains, as shown in Fig. 11(a). The enlarged image [Fig. 11 (b)] shows that these pores align parallel to the (111) plane of ZrC. On the basis of the orientation relationship between the ZrC and $Zr_2Al_3C_4$ [presented in Figs. 9(b) and 9(c)], the (111) plane of ZrC is parallel to the basal plane of $Zr_2Al_3C_4$. Thus, the aligned pores are parallel to the basal plane of $Zr_2Al_3C_4$, along which Al and C atoms could migrate outward easily. The coexistence of ZrC, Cu, and graphite is also detected by TEM in the sample annealed at 1050 °C [Fig. 11(c)]. In the enlarged image [Fig. 11(d)], the atomic arrangements of ZrC and Cu as well as the Moiré patterns formed by the overlap between them can be distinctly identified. Additionally, the lattice image of graphite and its FFT pattern are also presented. Significant disruption to the ordered graphite structure is evident.

3. Microstructure evolutionary stages of $Zr_2Al_3C_4$ in Cu

On the basis of the evidence presented previously, we propose that microstructure evolution of $Zr_2Al_3C_4$ in Cu

https://doi.org/10.1557/jmr.2010.52 Published online by Cambridge University Press

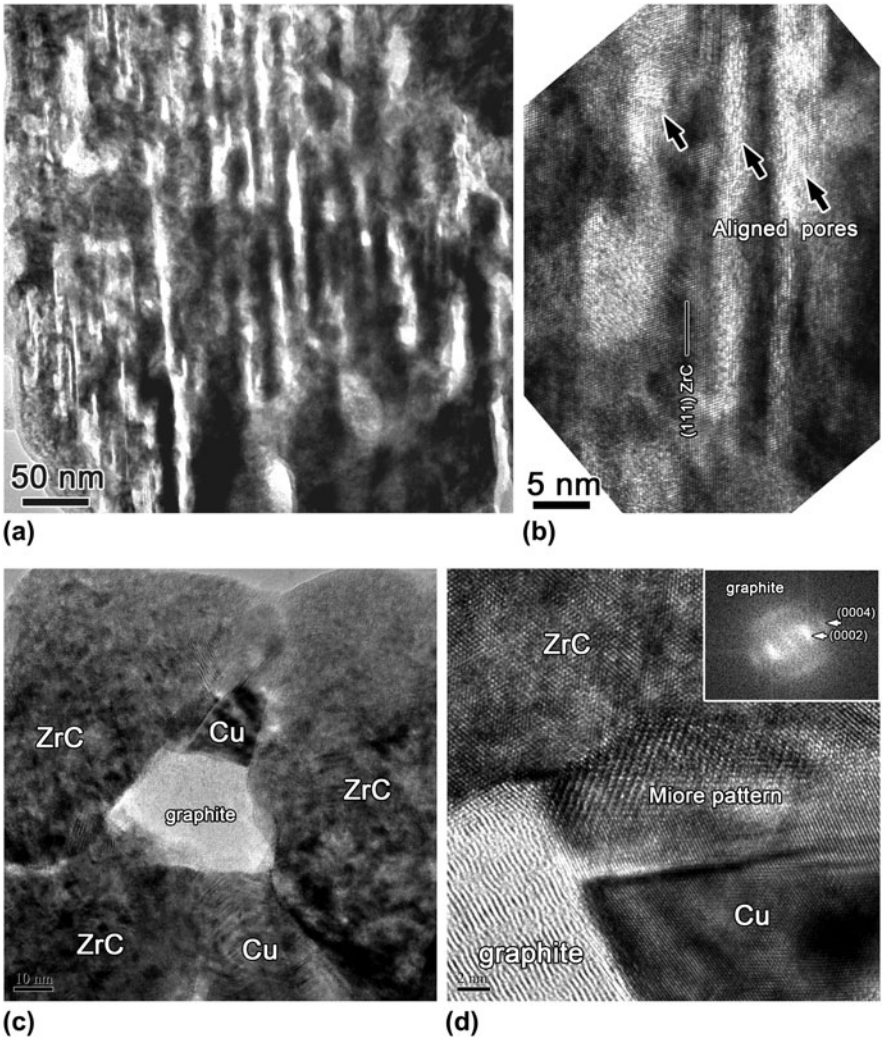


FIG. 11. (a) Typical morphology of ZrC grains in the sample annealed at 1050 °C, (b) enlarged image with aligned pores parallel to ZrC (111) plane, (c) coexistence of ZrC, Cu, and graphite in the sample annealed at 1050 °C, and (d) HRTEM image of the triple phase with the FFT image of graphite inserted.

matrix at high temperatures can be divided into the following stages. At high temperatures, the chemical affinity between Al and Cu acts as the driving force for $Zr_2Al_3C_4$ decomposition. Al atoms diffuse outward along the basal plane of $Zr_2Al_3C_4$, which leads to deintercalation of the entire Al–C unit in conjunction with volume shrinkage. Meanwhile, Cu diffuses into $Zr_2Al_3C_4$ grains along the channel formed by the volume shrinkage. During the mild reaction stage, only localized deintercalation of the Al–C unit occurs, resulting in the formation of a thin twinned ZrC and Cu platelets inside $Zr_2Al_3C_4$ grains [as illustrated in Fig. 12(a)]. Figure 12(b) indicates the next stage in the microstructure evolution. After the entire Al–C unit depletes from $Zr_2Al_3C_4$, disordered graphite and $ZrC_{0.5}$ twinning slabs form. The transformation from $Zr_2Al_3C_4$ to cubic $ZrC_{0.5}$ is accompanied by large volume shrinkage of ~52.5%. Therefore, aligned pores, which are parallel to the outward diffusion pathway of Al and C atoms, are observed inside ZrC grains. In the final stage of the microstructure evolution, recrystallization occurs, resulting in the rearrangement of C vacancies in $ZrC_{0.5}$. Highly twinned $ZrC_{0.5}$ and Cu–Al solid solution as well as graphite are the final products [Fig. 12(c)].

IV. DISCUSSION

Generally, Cu is chemically inert to most ceramics, such as SiC and Al_2O_3. In the as-synthesized composite, Cu matrix and these ceramic reinforcements are mechanically bonded. On the contrary, $Zr_2Al_3C_4$ can react with Cu at high temperatures. Investigation of the reaction between Cu and $Zr_2Al_3C_4$ promotes the understanding of the interfacial structure and chemistry in the composite. Therefore, it is possible to optimize the microstructure of Cu matrix composites by controlling the interfacial reaction. The microstructure, especially the interfacial structure, has a significant impact on the properties of the resultant composite.[45–47] In this section, the correlation

https://doi.org/10.1557/jmr.2010.52 Published online by Cambridge University Press

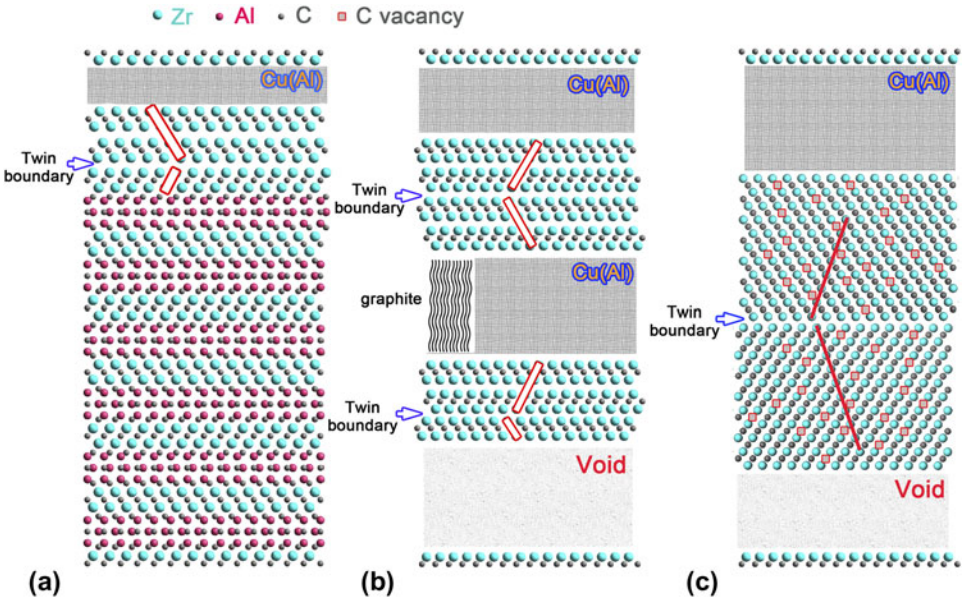


FIG. 12. Microstructure evolutionary stages of $Cu/Zr_2Al_3C_4$ composite.

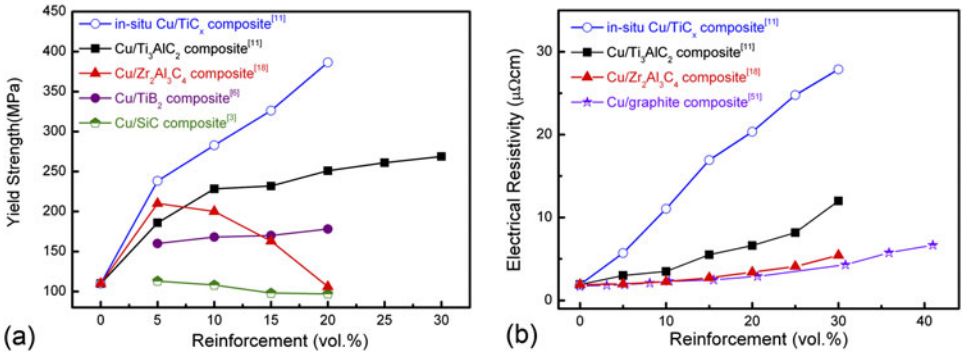


FIG. 13. (a) Yield strength of Cu matrix composites reinforced by in situ TiC_x,[11] Ti_3AlC_2,[11] $Zr_2Al_3C_4$,[19] TiB_2,[6] and SiC[3] particles, (b) electrical resistivity of in situ Cu/TiC_x,[11] Cu/Ti_3AlC_2,[11] Cu/Zr2Al3C4,[19] and Cu/graphite[51] composites.

between the interfacial structure and properties of Cu matrix composites will be discussed.

In Fig. 13(a), the yield strength of Cu matrix composites reinforced by in situ formed TiC_x,[11] Ti_3AlC_2,[11] $Zr_2Al_3C_4$,[19] TiB_2,[3] and SiC[6] particles, which are all fabricated by powder metallurgy methods, are summarized. The superior strengthening effect can be observed with the introduction of in situ TiC_x and Ti_3AlC_2 particles into Cu matrix compared to $Zr_2Al_3C_4$, TiB_2, and SiC particles. In the Cu/Ti_3AlC_2 composite, a high-strength interfacial layer composed of TiC_x and a Cu–Al solid solution forms between the matrix and reinforcement.[20] Thus, a notable improvement in yield strength is achieved by an effective load transfer through this strong interfacial layer. When the synthesis temperature increases to 1000 °C, Ti_3AlC_2 completely decomposes into TiC_x. A Cu matrix composite reinforced by in situ formed TiC_x is obtained[11] and this composite possesses higher mechanical properties than that of Cu/Ti_3AlC_2 composite, as summarized in Fig. 13(a). This example shows that by controlling the reaction between Ti_3AlC_2 and Cu matrix, the interfacial structure and the resultant properties of the composite can be improved. In $Cu/Zr_2Al_3C_4$, Cu/TiB_2, and Cu/SiC composites, reinforcements are mechanically bonded by Cu matrix. Under tensile tests, the applied load cannot be effectively transferred from matrix to reinforcement. Consequently, the strengthening effect is very limited.

As a member of layered ternary carbides, $Zr_2Al_3C_4$ exhibits a crystal structure similar to that of Ti_3AlC_2. The microstructure evolution of $Zr_2Al_3C_4$ in Cu at high temperatures is systematically studied in this work. However, no high-strength interfaces can be formed in the whole temperature range, which is attributed to the different bonding characteristics in $Zr_2Al_3C_4$ compared to Ti_3AlC_2. The crystal structure of Ti_3AlC_2 can be described as the intergrowth of Ti–C slabs and planar-packed Al atoms.[48,49] Recently, first-principle calculation has demonstrated that

https://doi.org/10.1557/jmr.2010.52 Published online by Cambridge University Press

Ti_2AlC (another member of Ti–Al–C system besides Ti_3AlC_2) presents an unusual Al-vacancy-bearing capability to form substoichiometry down to $Ti_2Al_{0.5}C$.[50] Experiments showed that the Ti_3AlC_2 grains maintain its symmetry and structure with partial depletion of Al from the ternary carbide.[20] When $Zr_2Al_3C_4$ reacts with Cu, both Al and C atoms deplete from the ternary carbide. The loss of an entire Al–C unit leads to collapse of the crystal structure even at a relatively low temperature, for example, 950 °C. When the temperature increases, all $Zr_2Al_3C_4$ converts into $ZrC_{0.54}$ with a volume shrinkage of 52.5% and aligned voids form inside ZrC grains.

Although no high-strength interfacial layer forms during the reaction between $Zr_2Al_3C_4$ and Cu, the relatively clean interface promotes the formation of continuous Cu network in Cu/$Zr_2Al_3C_4$ composite. Once the high conducting Cu network is spanning across the whole composite, ceramic particles remain as isolated clusters and the electrical resistivity approaches to the value of pure Cu. Experimentally, the electrical resistivity of Cu/$Zr_2Al_3C_4$ composite is significantly lower than that of in situ Cu/TiC_x and Cu/Ti_3AlC_2 composites, but comparable to that of Cu/graphite composites,[19,51,52] as indicated in Fig. 13(b). In Cu/Ti_3AlC_2 composites, the formation of a high-strength interfacial layer enables the load transfer and damages the Cu network in the composite. For in situ Cu/TiC_x composites, alternating distribution of Cu and TiC laminas destroy the continuous Cu network; the solid solution of Al in Cu matrix also increases the electrical resistivity. Therefore, at the same reinforcement content the electrical resistivity of the Cu/Ti_3AlC_2 composite is two to three times that of the Cu/$Zr_2Al_3C_4$ composite.

In terms of the microstructure-property relationship of Cu matrix composites reinforced by ceramic particles, the optimization of interfacial structure should be considered a tradeoff: the formation of a high-strength interfacial layer enables the load transfer in the composite and leads to notable improvement in mechanical behaviors, but this interfacial layer damages the continuous Cu network and results in the increase of electrical resistivity. To effectively transfer the load, a continuous and strong interface is required; to maintain the continuous Cu network, a discontinuous and moderate bonded interface is favored. Thus, an ideal interface in a metal matrix composite should facilitate wetting and bonding between the reinforcement and matrix to a desirable degree, which promotes load transfer as well as maintains the physical continuity in the composite.

In Cu matrix, the microstructure stability of layered ternary carbides, Ti_3AlC_2 and $Zr_2Al_3C_4$ for instance, varies significantly. There are more than 100 members in layered ternary carbides[14,49]; therefore, the microstructure of Cu matrix composites reinforced by layered ternary carbides is more flexible compared to the composites containing traditional ceramics such as Al_2O_3 and TiB_2. With the understanding of the reaction thermodynamics and kinetics, the optimum properties can be achieved, enabling practical applications particle-reinforced Cu matrix composites.

V. CONCLUSIONS

In this work, microstructure evolution of $Zr_2Al_3C_4$ in Cu is investigated by annealing the as-synthesized Cu/30 vol%$Zr_2Al_3C_4$ samples in the temperature range from 850 to 1050 °C. No reaction happens below 950 °C, i.e., Cu and $Zr_2Al_3C_4$ are mechanically bonded in the composite. In contact with Cu, decomposition of $Zr_2Al_3C_4$ occurs above 950 °C with the depletion of Al atoms that induces the deintercalation of the entire Al–C units from $Zr_2Al_3C_4$. Formation of ZrC and Cu platelets as well as a thin twinned ZrC slice inside $Zr_2Al_3C_4$ grains is also observed. With the increase of temperature to 1050 °C, severe reaction happens resulting in the coexistence of highly twinned ZrC and Cu lamellae. The transformation from $Zr_2Al_3C_4$ to twinned $ZrC_{0.54}$ is accompanied by large volume shrinkage of ~52.5%. Consequently, aligned pores form inside ZrC grains.

$Zr_2Al_3C_4$ exhibits higher stability in Cu matrix than that of Ti_3AlC_2 and Al_4C_3, due to the different atomic bonding characteristics and crystal structure. There are a considerable number of ternary carbides with layered structures similar to either Ti_3AlC_2 or $Zr_2Al_3C_4$; the structure stability of these layered ceramics in Cu matrix varies significantly. The mechanical and electrical properties of Cu matrix composites can be optimized by controlling the interfacial reaction between the Cu matrix and ceramic reinforcements.

ACKNOWLEDGMENTS

The authors thank Dr. Jian Luo from Clemson University, Clemson, SC, for revising the manuscripts and valuable suggestions. This work was supported by the National Outstanding Young Scientist Foundation for Y.C. Zhou under Grant No. 59925208, and Natural Sciences Foundation of China under Grant Nos. 90404027, 50772114, and 50832008.

REFERENCES

1. J.W. Kaczmar, K. Pirtrzak, and W. Wlosinski: The production and application of metal matrix composite materials. *J. Mater. Process. Technol.* **106**, 58 (2000).
2. L. Li, Y.S. Wong, J.Y.H. Fuh, and L. Lu: Effect of TiC in copper–tungsten electrodes on EDM performance. *J. Mater. Process. Technol.* **113**, 563 (2001).
3. S.C. Tjong and K.C. Lau: Tribological behaviour of SiC particle-reinforced copper matrix composites. *Mater. Lett.* **43**, 274 (2000).
4. K.M. Shu and G.C. Tu: The microstructure and the thermal expansion characteristics of Cu/SiC_p composites. *Mater. Sci. Eng., A* **349**, 236 (2003).
5. S.F. Moustafa, Z. Abdel-Hamid, and A.M. Abd-Elhay: Copper matrix SiC and Al_2O_3 particulate composites by powder metallurgy technique. *Mater. Lett.* **53**, 244 (2002).

https://doi.org/10.1557/jmr.2010.52 Published online by Cambridge University Press

6. S.C. Tjong and K.C. Lau: Abrasive wear behavior of TiB_2 particle-reinforced copper matrix composites. *Mater. Sci. Eng., A* **282**, 183 (2000).
7. J.C. Schuster and H. Nowotny: Investigations of the ternary systems (Zr, Hf, Nb, Ta)–Al–C. *Z. Metallkd.* **71**, 341 (1980).
8. N.T. Tzenov and M.W. Barsoum: Synthesis and characterization of Ti_3AlC_2. *J. Am. Ceram. Soc.* **83**, 825 (2000).
9. X.H. Wang and Y.C. Zhou: Microstructure and properties of Ti_3AlC_2 prepared by the solid–liquid reaction synthesis and simultaneous in situ hot pressing process. *Acta Mater.* **50**, 3143 (2000).
10. L.M. Peng: Fabrication and properties of Ti_3AlC_2 particulates reinforced copper composites. *Scr. Mater.* **56**, 729 (2007).
11. J. Zhang and Y.C. Zhou: Microstructure, mechanical, and electrical properties of Cu–Ti_3AlC_2 and in situ Cu–TiC_x composites. *J. Mater. Res.* **23**, 924 (2008).
12. Y. Zhang, Z.M. Sun, and Y.C. Zhou: Cu/Ti_3SiC_2 composite: A new electrofriction material. *Mater. Res. Innovations* **3**, 80 (1999).
13. J.Y. Wang, Y.C. Zhou, T. Liao, and Z.J. Lin: Trend in crystal structure of layered ternary *T*–Al–C carbides (*T* = Sc, Ti, Cr, Zr, Nb, Mo, Hf, W, and Ta). *J. Mater. Res.* **22**, 2685 (2007).
14. J.Y. Wang and Y.C. Zhou: Recent progress in theoretical prediction, preparation, and characterization of layered ternary transition-metal carbides. *Annu. Rev. Mater. Res.* **39**, 10 (2009).
15. T.M. Gesing and M. Jeitschko: The crystal structures of $Zr_3Al_3C_5$, $ScAl_3C_3$, and UAl_3C_3 and their relation to the structures of $U_2Al_3C_4$ and Al_4C_3. *J. Solid State Chem.* **140**, 396 (1998).
16. K. Fukuda, S. Mori, and S. Hashimoto: Crystal structure of $Zr_2Al_3C_4$. *J. Am. Ceram. Soc.* **88**, 3528 (2005).
17. L.F. He, Z.J. Lin, J.Y. Wang, Y.W. Bao, M.S. Li, and Y.C. Zhou: Synthesis and characterization of bulk $Zr_2Al_3C_4$ ceramic. *J. Am. Ceram. Soc.* **90**, 3687 (2007).
18. L.F. He, H.B. Zhong, J.J. Xu, M.S. Li, Y.W. Bao, J.Y. Wang, and Y.C. Zhou: Ultrahigh-temperature oxidation of $Zr_2Al_3C_4$ via rapid induction heating. *Scr. Mater.* **60**, 547 (2009).
19. J. Zhang, L.F. He, and Y.C. Zhou: Highly conductive and strengthened copper matrix composite reinforced by $Zr_2Al_3C_4$ particulates. *Scr. Mater.* **60**, 976 (2009).
20. J. Zhang, J.Y. Wang, and Y.C. Zhou: Structure stability of Ti_3AlC_2 in Cu and microstructure evolution of Cu–Ti_3AlC_2 composites. *Acta Mater.* **55**, 4381 (2007).
21. K. Suganuma, Y. Miyamoto, and M. Koizumi: Joining of ceramics and metals. *Annu. Rev. Mater. Sci.* **18**, 47 (1988).
22. R. Asthana and M. Singh: Joining of partially sintered alumina to alumina, titanium, Hastealloy and C–SiC composite using Ag–Cu brazes. *J. Eur. Ceram. Soc.* **28**, 617 (2008).
23. R. Asthana and M. Singh: Joining of ZrB_2-based ultra-high-temperature ceramic composites using Pd-based braze alloys. *Scr. Mater.* **61**, 257 (2009).
24. A. Avishai, C. Scheu, and W.D. Kaplan: Intergranular films at metal–ceramic interfaces: Part I—Interface structure and chemistry. *Acta Mater.* **53**, 1559 (2005).
25. I. Obinata and G. Wassermann: X-ray analysis of the solubility of aluminum in copper. *Naturwiss*. **21**, 382 (1933).
26. A.J. Bradley and H.J. Goldschmidt: An x-ray study of slowly cooled iron-copper-aluminium alloys—Part I. Alloys rich in iron and copper. *J. Inst. Met.* **65**, 389 (1939).
27. S.K. Pradhan and M. De: An x-ray determination of the thermal expansion of α-phase Cu–Al alloys at high temperature. *J. Appl. Crystallogr.* **21**, 980 (1988).
28. V. Ozoliņš and J. Häglund: First-principles study of effective cluster interactions and enthalpies of formation of substoichiometric VC_{1-x}. *Phys. Rev. B* **48**, 5069 (1993).
29. P.A. Korahavyi, L.V. Pourovokii, H.W. Hugoosson, A.V. Ruban, and B. Johansson: *Ab initio study of phase equilibria in TiC$_x$. Phys. Rev. Lett.* **88**, 15505 (2002).
30. H.W. Hugoosson, O. Eriksson, U. Jansson, and B. Johansson: Phase stabilities and homogeneity ranges in 4*d*-transition-metal carbides: A theoretical study. *Phys. Rev. B* **63**, 134108 (2001).
31. G.V. Samsonov, M.S. Koval'chenko, R.Ya. Petrykina, and V.Ya. Naumenko: Hot pressing of the transition metals and their carbides in their homogenity regions. *Powder Metall. Met. Ceram.* **9**, 713 (1970).
32. R.V. Sara: The system zirconium-carbon. *J. Am. Ceram. Soc.* **48**, 243 (1965).
33. A.C. Ferrari: Raman spectroscopy of graphene and graphite: Disorder, electron-phonon coupling, doping and nonadiabatic effects. *Solid State Commun.* **143**, 47 (2007).
34. L. Wu, L.F. He, Y.W. Bao, and Y.C. Zhou: Tribological properties of a $Zr_2Al_3C_4$ ceramic at ambient temperature. *J. Am. Ceram. Soc.* **92**, 141 (2009).
35. J. Robertson: Diamond-like amorphous carbon. *Mater. Sci. Eng., R* **37**, 129 (2002).
36. F. Tuinstra and J.L. Koening: Raman spectrum of graphite. *J. Chem. Phys.* **53**, 1126 (1970).
37. E. Parthé and B. Chabot: $Zr_2Al_3C_{5-x}$ and $Hf_2Al_3C_{5-x}$ described with higher symmetrical space group $P6_3/mmc$. *Acta Crystallogr., Sect. C: Cryst. Struct. Commun.* **44**, 774 (1988).
38. Z.J. Lin, M.J. Zhuo, L.F. He, Y.C. Zhou, M.S. Li, and J.Y. Wang: Atomic-scale microstructures of $Zr_2Al_3C_4$ and $Zr_3Al_3C_5$. *Acta Mater.* **54**, 3843 (2006).
39. J.S. Binford, Jr., J.M. Strohmenger, and T.H. Hebert: A modified drop calorimeter. The heat content of aluminum carbide and cobalt (II) fluoride above 25°. *J. Phys. Chem.* **71**, 2404 (1967).
40. J.C. Schuster: A reinvestigation of the thermal decomposition of aluminum carbide and the constitution of the Al–C system. *J. Phase Equilib*. **12**, 546 (1991).
41. C. Qiu and R. Metselaar: Solubility of carbon in liquid Al and stability of Al_4C_3. *J. Alloys Compd.* **216**, 55 (1994).
42. J.Y. Wang, Y.C. Zhou, Z.J. Lin, and T. Liao: First-principle investigation on chemical bonding and bulk modulus of the ternary carbide $Zr_2Al_3C_5$. *Phys. Rev. B* **72**, 052102 (2005).
43. J.Y. Wang, Y.C. Zhou, Z.J. Lin, T. Liao, and L.F. He: First-principles prediction of the mechanical properties and electronic structure of ternary aluminum carbide $Zr_3Al_3C_5$. *Phys. Rev. B* **73**, 134107 (2006).
44. T. Liao, J.Y. Wang, and Y.C. Zhou: Atomistic deformation modes and intrinsic brittleness of Al_4SiC_4: A first-principles investigation. *Phys. Rev. B* **74**, 174112 (2006).
45. M. Rühle: Structure and composition of metal/ceramic interfaces. *J. Eur. Ceram. Soc.* **16**, 353 (1996).
46. H. Zhang, K.T. Ramesh, and E.S.C. Chin: Effects of interfacial debonding on the rate-dependent response of metal matrix composites. *Acta Mater.* **53**, 4687 (2005).
47. V.A. Romanova, R.R. Balokhonov, and S. Schmauder: The influence of the reinforcing particle shape and interface strength on the fracture behavior of a metal matrix composite. *Acta Mater.* **57**, 97 (2009).
48. Y.C. Zhou, X.H. Wang, Z.M. Sun, and S.Q. Chen: Electronic and structural properties of the layered ternary carbide Ti_3AlC_2. *J. Mater. Chem.* **11**, 2335 (2001).
49. D. Music and J.M. Schneider: The correlation between the electronic structure and elastic properties of nanolaminates. *JOM* **59**, 60 (2007).
50. J.Y. Wang, Y.C. Zhou, T. Liao, J. Zhang, and Z.J. Lin: A first-principle investigation of the phase stability of Ti_2AlC with Al vacancies. *Scr. Mater.* **58**, 227 (2008).
51. J. Kovácõik and J. Bielek: Electrical conductivity of Cu/graphite composite material as a function of structural characteristics. *Scr. Mater.* **35**, 151 (1996).
52. A. Yeoh, J. Persad, and Z. Eliezer: Dimensional response of copper-graphite powder composites to sintering. *Scr. Mater.* **37**, 271 (1996).

https://doi.org/10.1557/jmr.2010.52 Published online by Cambridge University Press